

Ultra extreme high-frequency-peaked BL Lacs: a potential population of MeV synchrotron blazars?

A. Sciacaluga¹, F. Tavecchio¹, T. Sbarrato¹, and G. Bonnoli¹

INAF – Osservatorio Astronomico di Brera, Via E. Bianchi 46, I-23807 Merate, Italy
e-mail: alberto.sciacaluga@inaf.it

ABSTRACT

We investigate the potential existence of a new population of BL Lacs, called ultra extreme high-energy-peaked BL Lacs (UEHBLs), whose synchrotron emission component peaks in the MeV band, extending the blazar sequence beyond its current limit. To model the spectral energy distribution of these new sources, we apply the hybrid shock-turbulence acceleration framework previously developed for extreme high-frequency-peaked BL Lacs. We present three representative realizations that produce synchrotron peaks between 0.2 and 2 MeV and evaluate their multiwavelength signatures. Our results show that UEHBLs would be undetectable with current GeV (Fermi) and future TeV (CTA) facilities due to severe Klein–Nishina suppression of inverse Compton scattering, but are ideal targets for proposed MeV missions such as COSI, AMEGO-X, and e-ASTROGAM. We further identify a sample of hard X-ray sources from the Swift-BAT catalogs that exhibit the expected spectral properties of UEHBLs, potentially representing the first observational hints of this population. If confirmed, UEHBLs would provide unique insight into particle acceleration in relativistic jets, imposing strong constraints on the maximum achievable electron energies. We also discuss the expected polarization and variability signatures, including the possibility of synchrotron-driven thermal instabilities leading to MeV flares. These findings underscore the critical importance of the MeV band for discovering and characterizing the most extreme accelerators among blazars.

Key words. galaxies: jets – radiation mechanisms: nonthermal

1. Introduction

Relativistic jets launched by active galactic nuclei (AGN) emit radiation across the entire electromagnetic spectrum, from radio waves to gamma rays, and possibly also produce neutrinos. These jets provide unique laboratories to study black hole physics, particle acceleration, and high-energy emission processes (e.g., Blandford et al. 2019). Blazars are among the best targets for investigating jet physics. They are radio-loud AGN whose relativistic jet is oriented close to our line of sight. Because of this alignment, the jet nonthermal emission is strongly amplified by relativistic beaming and dominates the spectral energy distribution (SED) (e.g., Romero et al. 2017; Böttcher 2019).

The SED of a blazar typically exhibits two broad humps. The low-energy hump peaks between the infrared and X-ray bands and is generally attributed to synchrotron emission from relativistic leptons. The high-energy hump, which peaks from MeV to TeV energies, is less well understood, and its origin remains debated. In the leptonic scenario, it is explained as the result of inverse Compton scattering, where relativistic leptons upscatter photons from either their own synchrotron radiation (synchrotron self-Compton or SSC) or from external radiation fields (e.g., Maraschi et al. 1992; Sikora et al. 1994; Ghisellini et al. 1998). Alternatively, hadronic models attribute the high-energy component to processes involving relativistic protons, such as direct proton synchrotron emission or synchrotron radiation from secondary particles produced in hadronic interactions (e.g., Cerruti 2020; Sol & Zech 2022). The hadronic picture is supported by the possible association of some blazars with high-energy neutrino detections (e.g., IceCube Collaboration et al. 2018).

The positions of the two SED peaks are used to classify blazars, giving rise to the so-called blazar sequence, in which the peak frequencies anticorrelate with the bolometric luminosity (Fossati et al. 1998; Donato et al. 2001; Ghisellini et al. 2017). At the low-luminosity end of this sequence lie extreme high-frequency-peaked BL Lacs (EHBLs), namely the most efficient particle accelerators among blazars (for a review, Biteau et al. 2020).

In the seminal paper by Ghisellini (1999), the author proposed extending the blazar sequence beyond its previously assumed limits, suggesting the existence of a new BL Lacs population whose synchrotron spectrum peaks in the MeV band. In principle, there is no strict theoretical bound on the maximum synchrotron photon energy, except for the so-called synchrotron burn-off limit. If nonthermal particles are accelerated at shocks (or, more generally, by a gyroresonant process), the minimum acceleration timescale corresponds to the gyration time, $t_g = 2\pi r_g/c$, where r_g is the particle gyroradius. This process is constrained by synchrotron cooling, which imposes an upper limit on the achievable photon energy that is independent of the magnetic field strength. For a relativistically beamed source, the maximum synchrotron photon energy can reach $\sim 25\delta$ MeV, comfortably exceeding the energies observed in EHBLs (e.g., Guilbert et al. 1983; de Jager et al. 1996). Specifically for high-energy BL Lacs, assuming that the acceleration timescale is a multiple of the gyration time, $t_{\text{acc}} = \eta t_g$, leads to very large values, $\eta \sim 10^5$, implying that shocks are rather slow accelerators (e.g., Inoue & Takahara 1996; Garson et al. 2010).

A natural starting point for modeling MeV-peaking BL Lacs is one of the competing frameworks proposed for EHBLs. Owing to their peculiar spectral features, namely the large separa-

tion between the two peaks and their steep gamma-ray spectrum, the standard one-zone leptonic model typically requires unusually low magnetic fields ($B < 10$ mG) and very high average electron Lorentz factors ($\bar{\gamma} \sim 10^3 - 10^4$). These values place EHBLs as clear outliers with respect to the parameter ranges inferred for other BL Lacs (Tavecchio et al. 2010; Kaufmann et al. 2011; Costamante et al. 2018). To account for these differences, several alternative scenarios have been proposed, including a Maxwellian-like electron distribution (Lefa et al. 2011), a beam of high-energy hadrons (Essey & Kusenko 2010), emission from a large-scale jet (Aharonian et al. 2008), lepto-hadronic models (Cerruti et al. 2015), and multiple shock acceleration (Zech & Lemoine 2021).

In Sciacaluga & Tavecchio (2022) and Sciacaluga et al. (2024), we presented a novel framework for EHBLs, based on the combined action of shock and turbulence acceleration. In this scenario, non-thermal leptons are initially accelerated by a shock and subsequently energized by the downstream turbulence.

All EHBL models can, in principle, be extended to even higher energies, potentially giving rise to a new population of BL Lacs. If these extreme sources are indeed observed, they would provide a unique laboratory for testing competing acceleration and emission scenarios.

BL Lacs whose synchrotron hump peaks in the MeV band, here termed ultra extreme high-frequency-peaked BL Lacs (UEHBLs), would be ideal targets for the upcoming missions designed to explore this energy range (for a review about extragalactic sources, Sbarrato et al. 2025). Historically, the 0.1 MeV–100 MeV band has been poorly sampled: only a few missions have partially covered it and with limited sensitivity. For this reason, this portion of the electromagnetic spectrum is commonly referred to as the “MeV gap.” In recent years, several satellites have been proposed to bridge this gap, spanning small, medium, and large-scale missions, such as COSI (Tomsick & COSI Collaboration 2022), AMEGO-X (Caputo et al. 2022), and e-ASTROGAM (de Angelis et al. 2018).

If UEHBLs do exist, they may have already left observable signatures in neighboring energy bands. For instance, in the hard X-rays, satellites such as Swift-BAT (Barthelmy et al. 2005) provide excellent sky coverage and sensitivity. Interestingly, the BAT catalogs include a number of sources without clear counterparts, which could represent promising candidates for this hypothesized BL Lac population (Oh et al. 2018; Lien et al. 2025).

The paper is organized as follows. In Section 2, we describe the hybrid shock–turbulence acceleration model. Section 3 reports and discusses three representative realizations of the model. In Section 4, we examine the potential temporal and polarimetric characteristics of UEHBLs and discuss the implications for possible acceleration and emission mechanisms. Throughout the paper, the following cosmological parameters are assumed: $H_0 = 70 \text{ km s}^{-1} \text{ Mpc}^{-1}$, $\Omega_M = 0.3$, $\Omega_\Lambda = 0.7$.

2. Shock-turbulence model

In this section, we briefly describe our shock-turbulence acceleration model, one of the possible EHBL models that could be extended to UEHBLs. For more details, refer to Sciacaluga & Tavecchio (2022) and Sciacaluga et al. (2024).

As mentioned in the introduction, Zech & Lemoine (2021) propose a model based on multiple shock acceleration. Their idea relies on the fact that recollimation (or, more generally, standing) shocks occur in series, as demonstrated by several 2D fluid simulations (e.g., Gomez et al. 1995; Mizuno et al.

2015). However, 3D fluid simulations reveal that the flow is subject to instabilities, which evolve into turbulence and ultimately disrupt the cycle of recollimation and reflection shocks (e.g., Matsumoto & Masada 2013; Gourgouliatos & Komissarov 2018; Boula et al. 2025; Costa et al. 2025; Hu et al. 2025). For this reason, we suppose that particles are first accelerated by a shock and then further energized by the downstream turbulence.

We assume that the emitting region is the turbulent downstream of a recollimation shock and we adopt a leaky-box, spatially averaged approach, so that our scenario is effectively a one-zone leptonic model. The temporal evolution of the electrons and turbulence is governed by two coupled Fokker–Planck equations (e.g., Eilek 1979; Miller et al. 1996; Kakuwa 2016; Gong et al. 2025),

$$\begin{cases} \frac{\partial f}{\partial t} = \frac{1}{p^2} \frac{\partial}{\partial p} \left[p^2 D_p \frac{\partial f}{\partial p} + p^2 \left(\frac{\partial p}{\partial t} \right)_{\text{rad}} f \right] - \frac{f}{t_{\text{esc}}} + I_f \\ \frac{\partial W}{\partial t} = \frac{\partial}{\partial k} \left[k^2 D_k \frac{\partial}{\partial k} \left(\frac{W}{k^2} \right) \right] - \frac{W}{t_{\text{dam}}} + I_w \end{cases}, \quad (1)$$

where p is the electron momentum, k the fluctuation wavenumber, $f(p, t)$ the electron isotropic phase-space density, and $W(k, t)$ is the turbulence energy density per unit of wavenumber. Eq. (1) describes the interplay between particle processes (resonant acceleration, cooling, escape, and injection) and turbulence processes (cascading, damping, and injection). All quantities are defined in the comoving frame of the emission region. The expressions for particle acceleration and turbulence damping are derived from quasilinear theory, though alternative approaches exist (e.g., Lemoine et al. 2024).

The diffusion coefficient of electrons is given by

$$D_p = \frac{p^2 \beta_a^2 c}{U_B r_g^2} \int_{k_{\text{res}}} \frac{W_B}{k} dk, \quad (2)$$

where β_a is the dimensionless Alfvén speed, $U_B = B^2/8\pi$ the magnetic energy density, r_g the electron gyroradius, $W_B \approx W/2$ the magnetic component of the turbulence energy spectrum, and $k_{\text{res}} = 1/r_g$ the resonant wavenumber.

The electron cooling term accounts for both synchrotron and inverse Compton contributions, following standard formulae from the literature (e.g., Jones 1965; Chiaberge & Ghisellini 1999).

The electron escape time is equal to

$$t_{\text{esc}} = \frac{R}{c} + \frac{R^2}{\kappa_{\parallel}}, \quad (3)$$

where R is the emission region radius and $\kappa_{\parallel} = cr_g/9\zeta(k_{\text{res}})$ is the spatial diffusion coefficient along the magnetic field, with $\zeta(k) = kW_B/U_B$ the relative amplitude of the turbulent magnetic field energy density for a given k . When the mean free path is large, the escape time is essentially the geometric escape time. Conversely, when the mean free path is small, turbulence traps particles in the emission region, leading to a longer escape time.

Before gaining energy through turbulence, particles are initially accelerated at the shock, which thus acts as the injector for the emission region. The electron injection number density per unit of Lorentz factor I_n is given by

$$I_n = I_{n,0} \gamma^{-2} e^{-\frac{\gamma}{\gamma_{\text{cut}}}} \quad \text{with } \gamma > \gamma_{\text{min}}, \quad (4)$$

where γ denotes the electron Lorentz factor, $I_{n,0}$ is the injection normalization, and $\gamma_{\text{min}} = 10^3$ and $\gamma_{\text{cut}} = 10^5$ are respectively

the minimum and cutoff Lorentz factor of the injected electron distribution. Note that $I_n = 4\pi p^2 m_e c I_f$, where I_f is the corresponding injection distribution in phase space. The slope and cutoff of the injection are determined from recent simulations of diffusive shock acceleration for weakly magnetized shocks (e.g., [Vanthieghem et al. 2020](#); [Zech & Lemoine 2021](#)). The injection is normalized to the injected electron power P_n ,

$$P_n = V \int \gamma m_e c^2 I_n d\gamma, \quad (5)$$

where $V = 10\pi R^3$ is the emission region volume, modeled as a cylinder with radius R and length $10R$. The length of the emission volume, related to the region where the instability develops and triggers turbulence in the plasma, is roughly estimated on fluid simulations (e.g., [Matsumoto et al. 2021](#); [Boula et al. 2025](#); [Costa et al. 2025](#)). We expect that within such a distance, both the magnetic field decay and the adiabatic losses effectively quench the emission.

Assuming Kolmogorov phenomenology, the diffusion coefficient of turbulence is given by

$$D_k = k^3 \beta_a c \sqrt{\frac{kW}{2U_B}}. \quad (6)$$

Without strong damping, and given this diffusion coefficient with continuous injection, $W(k)$ would evolve toward the standard Kolmogorov spectrum, $W(k) \propto k^{-5/3}$ ([Zhou & Matthaeus 1990](#)).

The turbulence damping time is equal to

$$t_{\text{dam}} = -\frac{4\pi e^2 \beta_a^2}{m_e c k} \int_{\gamma_{\text{res}}} \gamma^2 \frac{\partial}{\partial \gamma} \left(\frac{n_e}{\gamma^2} \right) d\gamma, \quad (7)$$

where $n_e(\gamma) = 4\pi m_e c p^2 f(p)$ is the electron number density per unit of Lorentz factor and γ_{res} is the resonant Lorentz factor, defined as $k = 1/r_g(\gamma_{\text{res}})$. Damping is determined by enforcing energy conservation, so that the energy driving electron acceleration is removed from the turbulence.

The turbulence injection term is equal to

$$I_W = I_{W,0} \delta(k - k_0), \quad (8)$$

where δ is the Dirac function, $I_{W,0}$ the normalization, and $k_0 = 1/L$ the injection wavenumber, with $L = R/10$. The injection is normalized to the injected turbulence power P_w :

$$P_w = V \int I_W dk. \quad (9)$$

The radiative output of the emission region is computed using the SSC model, following the standard formulae in the literature (e.g., [Jones 1968](#); [Blumenthal & Gould 1970](#); [Ghisellini et al. 1988](#)). For the treatment of relativistic beaming, we adopt the usual blob amplification formula ([Sikora et al. 1997](#); [Zech & Lemoine 2021](#)).

We employed the Chang–Cooper algorithm ([Chang & Cooper 1970](#)) on a logarithmic grid, using 20 points per decade for momentum, wavenumber, and frequency. The system was evolved over a time interval of $10R/c$ with 100 time steps.

3. Results

In this section, we discuss some examples of realizations of the hybrid shock–turbulence model that produce BL Lacs with spectral peak in the MeV band. In Fig. 1, we present three representative realizations. The model depends on six parameters: the emission region radius R , the dimensionless Alfvén speed β_a , the magnetic field strength B , the injected electron power P_e , the injected turbulence power P_w , and the relativistic Doppler factor $\mathcal{D} = [\Gamma(1 - \beta \cos \theta_v)]^{-1}$ (where Γ and β denote the bulk Lorentz factor and the dimensionless velocity of the fluid, respectively, while θ_v is the observer’s viewing angle). The parameter sets corresponding to the three realizations are summarized in Tab. 1. In all cases, the redshift is fixed at $z = 0.14$, matching that of the prototypical EHBL 1ES 0229+200 ([Woo et al. 2005](#)). In addition to the input parameters, the table also lists two derived quantities used to check model consistency: the magnetization, $\sigma = \beta_a^2/(1 - \beta_a^2)$, and the relative amplitude of turbulent magnetic fluctuations, $\delta B/B = (\int W_B dk/U_B)^{1/2}$.

Table 1. Physical parameters and derived quantities for the three modeled cases

Parameter	Case A	Case B	Case C
Emission region radius [cm]	1.0×10^{16}	1.0×10^{16}	2.0×10^{16}
Magnetic field [G]	1.7×10^{-2}	3.0×10^{-2}	3.0×10^{-2}
Dimensionless Alfvén speed	2.0×10^{-1}	2.0×10^{-1}	2.0×10^{-1}
Injected electron power [erg/s]	1.0×10^{37}	3.0×10^{36}	3.0×10^{36}
Injected turbulence power [erg/s]	1.0×10^{40}	1.0×10^{40}	3.0×10^{39}
Relativistic Doppler factor	1.6×10^1	2.0×10^1	2.5×10^1
Magnetization	4.2×10^{-2}	4.2×10^{-2}	4.2×10^{-2}
Turbulence relative magnitude	2.0×10^{-1}	1.4×10^{-1}	9.4×10^{-2}

In all three cases, the emission region is assumed to be at sub-parsec scales, as is plausible for BL Lacs ([Tavecchio et al. 1998, 2010](#)). The dimensionless Alfvén speed is fixed to ensure low magnetization, which makes shock acceleration efficient and favors the development of instabilities and turbulence in the downstream region (e.g., [Vanthieghem et al. 2020](#); [Matsumoto et al. 2021](#)). The remaining parameters are varied as needed. However, since we adopt the quasilinear approximation, we have verified that the relative turbulence amplitude remains small, i.e., $\delta B/B \ll 1$. The time evolution of the electron and turbulence spectra for Case A is reported in Appendix A. Cases B and C exhibit similar behavior and are therefore not shown.

Case A provides the most efficient acceleration, with the low-energy bump peaking at ~ 2 MeV. In the MeV band, the low energy-peak is fully detectable by AMEGO-X and e-ASTROGAM, with the latter also able to detect Case A beyond the peak. COSI cannot observe the source within its nominal mission lifetime, namely 2 years, although Case A would become detectable if the mission were extended. Detection by COSI would also be possible in the event of a strong flare. Although EHBLs, the closest known class of sources to those hypothesized here, do not exhibit strong flaring at the frequencies corresponding to the low-energy bump, radiative thermal instabilities could trigger such flares, as discussed in Section 4.

Potential constraints could arise from the hard X-ray band. As mentioned in the introduction, valuable information may come from Swift-BAT, which operates in the hard X-rays and offers excellent sky coverage. Recently published BAT catalogs ([Oh et al. 2018](#); [Lien et al. 2025](#)) contain several candidates that may represent UEHBLs. To identify such candidates, we filtered the BAT catalogs with the following criteria: i) integrated flux in the BAT band above 10^{-11} erg cm $^{-2}$ s $^{-1}$, ii) photon index

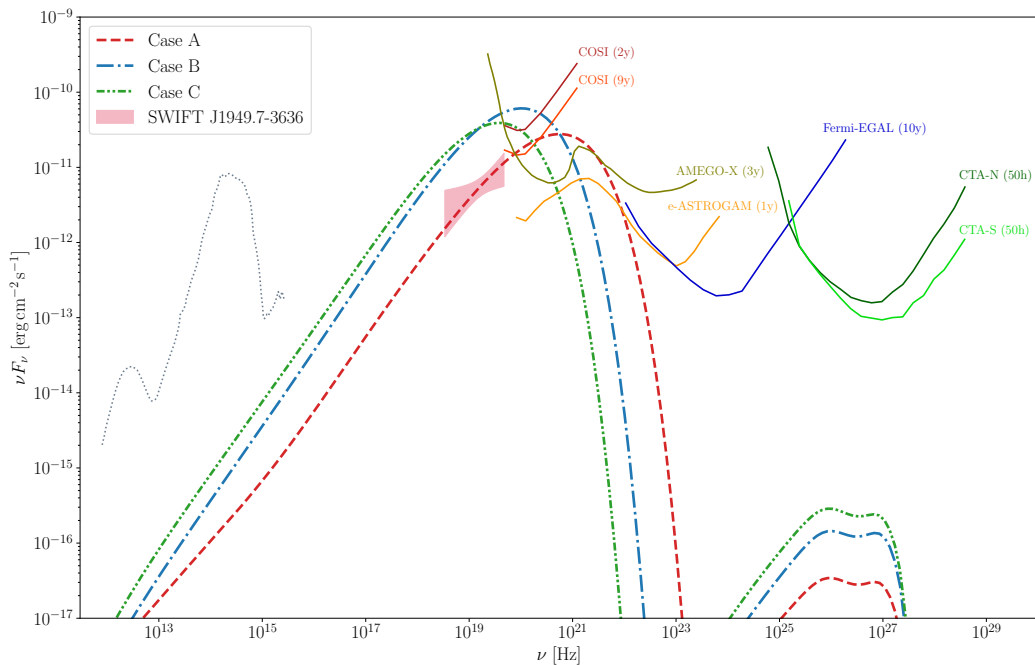


Fig. 1. SEDs for three model realizations: Case A (dashed red), Case B (dash-dotted blue), and Case C (dash-double-dotted green), including attenuation from extragalactic background light (EBL) absorption (Franceschini & Rodighiero 2017). Solid dark/light red lines show COSI 2- and 9-year sensitivities (Tomsick & COSI Collaboration 2022); dark yellow and orange lines show AMEGO-X (3 yr; Caputo et al. 2022) and e-ASTROGAM (1 yr; de Angelis et al. 2018) sensitivities. The Fermi-LAT 10-year extragalactic sensitivity (taken from https://www.slac.stanford.edu/exp/glast/groups/canda/lat_Performance.htm) is shown in solid blue, and CTA North/South 50-hour sensitivities (taken from <https://www.ctao.org/for-scientists/performance/>) in dark/light green. The red shaded region marks the BAT-band flux of Swift J1949.7–3636 (Lien et al. 2025), a candidate MeV-peaking BL Lac. For reference, a SED template of a giant elliptical galaxy taken from (Silva et al. 1998) is displayed in dotted grey, renormalized to the magnitude of the host galaxy of 1ES 0229+200 (Costamante et al. 2018).

$\Gamma < 1.5$, iii) likely extragalactic origin (defined by a Galactic latitude $|b| > 10^\circ$), iv) absence of a clear counterpart in the soft X-ray and optical bands. The requirements on the flux and index in the hard X-rays were imposed to identify sources that could be detectable by the next generation MeV telescopes. Applying these requirements, we identified ten possible sources according to the catalogs classification. Their number might drop to six, due to possible updated X-ray counterpart candidates (see Appendix B for further details). In Fig. 1, we plot the integrated BAT flux of one of the candidates, SWIFT J1949.7-3636. All BAT candidates lack a soft X-ray counterpart that allows a clear association with sources in optical catalogs. This is consistent with Case A, in which the soft X-ray flux is close to the sensitivity limit of current soft X-ray satellites. A potential approach to identifying a soft X-ray counterpart would be to perform a deep observation of the BAT error region using a soft X-ray telescope with a sufficiently large field of view, such as Swift-XRT (Burrows et al. 2005) and XMM-Newton (Jansen et al. 2001). In the event of multiple detections, spectral characteristics (e.g., a hard photon index) could help discriminate among the possible candidates. Note that these candidates could be FSRQs with their high-energy peak located in the MeV band. In this scenario, BAT would be detecting the rising part of the high-energy component. However, UEHBLs and MeV FSRQs are easily distinguishable. First, given a soft X-ray detection providing better localization, the optical counterpart should present broad emission lines in the case of FSRQs. Second, MeV FSRQs after the peak typically exhibit a power law tail extending into the GeV band, which should be detectable by Fermi.

The Case A parameters were selected to ensure consistency with the BAT data, but this requirement is highly restrictive. For realizations B and C, we therefore chose not to impose this constraint. From a theoretical perspective, there is no strict limitation on the properties of potential MeV BL Lacs, and intermediate cases between EHBLS and Case A should, in principle, also be possible. Moreover, as previously highlighted, these sources may not remain stable over time. Case A is consistent with a BAT source that has been monitored for 157 months. However, during this period, the source may have experienced flaring episodes, during which its brightness exceeded the average flux measured by BAT.

Case B has a low-energy bump peaking at ~ 0.5 MeV and it is the brightest candidate in the MeV band, potentially detectable by COSI within its nominal mission lifetime. Case C, with a peak at 0.2 MeV, represents the scenario most closely resembling EHBLS. While COSI could still detect Case C within its lifetime, the signal would lie near the edge of its sensitivity range, allowing observation only just beyond the peak. Thanks to their superior sensitivities, AMEGO-X and e-ASTROGAM would be able to probe both the peak and higher energies in Cases B and C.

All three cases are not observable by Fermi or CTA due to the severe suppression of the scattering cross section in the Klein–Nishina regime, assuming a full leptonic scenario (see Section 4 for further details on a possible hadronic component).

Finally, note that in all three cases the optical band is dominated by the galaxy emission, even more than in EHBLS, as shown in Fig. 1. A more accurate localization, for example us-

ing soft X-ray observations, would make it possible to detect the host galaxy of these sources.

4. Discussion

In this paper, we demonstrated that the hybrid shock–turbulence scenario, one of the possible models for EHBLs, can also account for UEHBLs. We presented three representative model realizations and discussed their detectability with proposed MeV observatories as well as with existing telescopes at other wavelengths. In addition, we identified ten potential candidates from the BAT catalogs.

Proposed MeV satellites such as COSI, AMEGO-X, and e-ASTROGAM would be essential for detecting these new sources. Their observations would provide valuable insights into particle acceleration. Previous studies have already shown that MeV observations of powerful FSRQ (sources at the opposite extreme of the blazar sequence with respect to EHBLs) could reveal, besides the standard non-thermal power law, the presence of a thermal component in the particle spectrum, which would point to shocks as the underlying acceleration mechanism (Tavecchio et al. 2025). On the other hand, the detection of BL Lacs peaking in the MeV band would imply that electrons can achieve extremely high Lorentz factors, a condition that could help further discriminate among the different particle acceleration mechanisms proposed in the literature. Conversely, a non-detection of such sources could be interpreted in two ways. First, particle acceleration, regardless of the underlying mechanism, must proceed relatively slowly, as discussed in Section 1. Second, UEHBLs may simply be too faint to be detected by the proposed MeV missions.

Aside from the spectral properties of UEHBLs, we are also interested in their polarimetric and temporal features. In the MeV band, we expect relatively high polarization degrees ($\geq 40\%$), following the trend observed in HBLs and EHBLs (e.g., Di Gesu et al. 2022; Liodakis et al. 2022; Ehlert et al. 2023; Kouch et al. 2024), where the polarization is strongly chromatic, i.e., the degree of polarization increases with frequency. Based on the flux predicted by our model (excluding strong flaring states), the polarization of UEHBLs would remain undetectable for COSI and AMEGO-X, while e-ASTROGAM could potentially measure it, depending on the actual polarization degree.

It is interesting to remark that UEHBLs could represent an exceptional class of sources. In fact, contrary to standard blazars, their emission would be dominated by synchrotron radiation, since inverse Compton contribution is strongly quenched by Klein-Nishina suppression. This peculiarity could potentially have an impact on the variability properties of these sources. Indeed, a source dominated by the pressure of non-thermal electrons and whose cooling is dominated by synchrotron losses could be subject to the radiative thermal instability discussed by Marscher (1980). A small increase of the magnetic field in limited portions of the flow can in fact lead to a collapse of the region due to the increased cooling rate of the relativistic electrons and consequent loss in pressure. The rapid radiative losses suffered by the electrons during the compression would produce a rapid increase of the emissivity, with flares potentially detectable in the MeV band.

As already outlined, in a purely leptonic scenario the inverse Compton emission is expected to be suppressed, since most electrons scatter photons in the Klein–Nishina regime. Consequently, as illustrated in Fig. 1, UEHBLs should remain undetectable by CTA. However, we cannot exclude that other mechanisms can result in a detectable flux even at these energies. First,

the emission could originate from a nonthermal hadronic component producing synchrotron radiation at TeV energies (e.g., Mannheim 1993; Aharonian 2000; Mücke & Protheroe 2001). Alternatively, a second emission region further downstream in the jet might exist, where nonthermal electrons generate infrared/radio photons. These photons could then be upscattered by the nonthermal electrons in the primary emission region in the Thomson regime, giving rise to a bright inverse Compton bump detectable by CTA. Variability studies could help discriminate between these two scenarios. Rapid variability on timescales of hours would disfavor the hadronic model, since the synchrotron cooling timescale for protons is expected to be orders of magnitude longer.

Acknowledgements. This work has been funded by ASI under contract 2024-11-HH.0. We acknowledge financial support from an INAF Theory Grant 2024 (PI F. Tavecchio) and the European Union-Next Generation EU, PRIN 2022 RFF M4C21.1 (2022C9TNNX).

References

- Aharonian, F. A. 2000, *New A*, 5, 377
 Aharonian, F. A., Khangulyan, D., & Costamante, L. 2008, *MNRAS*, 387, 1206
 Barthelmy, S. D., Barbier, L. M., Cummings, J. R., et al. 2005, *Space Sci. Rev.*, 120, 143
 Biteau, J., Prandini, E., Costamante, L., et al. 2020, *Nature Astronomy*, 4, 124
 Blandford, R., Meier, D., & Readhead, A. 2019, *ARA&A*, 57, 467
 Blumenthal, G. R. & Gould, R. J. 1970, *Reviews of Modern Physics*, 42, 237
 Böttcher, M. 2019, *Galaxies*, 7, 20
 Boula, S., Tavecchio, F., Bodo, G., et al. 2025, arXiv e-prints, arXiv:2510.01742
 Burrows, D. N., Hill, J. E., Nousek, J. A., et al. 2005, *Space Sci. Rev.*, 120, 165
 Caputo, R., Ajello, M., Kierans, C. A., et al. 2022, *Journal of Astronomical Telescopes, Instruments, and Systems*, 8, 044003
 Cerruti, M. 2020, *Galaxies*, 8, 72
 Cerruti, M., Zech, A., Boisson, C., & Inoue, S. 2015, *MNRAS*, 448, 910
 Chang, J. S. & Cooper, G. 1970, *Journal of Computational Physics*, 6, 1
 Chiaberge, M. & Ghisellini, G. 1999, *MNRAS*, 306, 551
 Costa, A., Bodo, G., Tavecchio, F., et al. 2025, arXiv e-prints, arXiv:2503.18602
 Costamante, L., Bonnoli, G., Tavecchio, F., et al. 2018, *MNRAS*, 477, 4257
 de Angelis, A., Tatishcheff, V., Grenier, I. A., et al. 2018, *Journal of High Energy Astrophysics*, 19, 1
 de Jager, O. C., Harding, A. K., Michelson, P. F., et al. 1996, *ApJ*, 457, 253
 Di Gesu, L., Donnarumma, I., Tavecchio, F., et al. 2022, *ApJ*, 938, L7
 Donato, D., Ghisellini, G., Tagliaferri, G., & Fossati, G. 2001, *A&A*, 375, 739
 Ehlert, S. R., Liodakis, I., Middei, R., et al. 2023, *ApJ*, 959, 61
 Eilek, J. A. 1979, *ApJ*, 230, 373
 Essey, W. & Kusenko, A. 2010, *Astroparticle Physics*, 33, 81
 Fossati, G., Maraschi, L., Celotti, A., Comastri, A., & Ghisellini, G. 1998, *MNRAS*, 299, 433
 Franceschini, A. & Rodighiero, G. 2017, *A&A*, 603, A34
 Garson, III, A. B., Baring, M. G., & Krawczynski, H. 2010, *ApJ*, 722, 358
 Ghisellini, G. 1999, *Astroparticle Physics*, 11, 11
 Ghisellini, G., Celotti, A., Fossati, G., Maraschi, L., & Comastri, A. 1998, *MNRAS*, 301, 451
 Ghisellini, G., Guilbert, P. W., & Svensson, R. 1988, *ApJ*, 334, L5
 Ghisellini, G., Righi, C., Costamante, L., & Tavecchio, F. 2017, *MNRAS*, 469, 255
 Gomez, J. L., Marti, J. M. A., Marscher, A. P., Ibanez, J. M. A., & Marcaide, J. M. 1995, *ApJ*, 449, L19
 Gong, X.-W., Liu, R.-Y., Zhang, Z.-L., Asano, K., & Lemoine, M. 2025, *ApJ*, 989, 99
 Gourgouliatos, K. N. & Komissarov, S. S. 2018, *Nature Astronomy*, 2, 167
 Guilbert, P. W., Fabian, A. C., & Rees, M. J. 1983, *MNRAS*, 205, 593
 Hu, X.-F., Mizuno, Y., & Fromm, C. M. 2025, *A&A*, 693, A154
 IceCube Collaboration, Aartsen, M. G., Ackermann, M., et al. 2018, *Science*, 361, eaat1378
 Inoue, S. & Takahara, F. 1996, *ApJ*, 463, 555
 Jansen, F., Lumb, D., Altieri, B., et al. 2001, *A&A*, 365, L1
 Jones, F. C. 1965, *Physical Review*, 137, 1306
 Jones, F. C. 1968, *Physical Review*, 167, 1159
 Kakuwa, J. 2016, *ApJ*, 816, 24
 Kaufmann, S., Wagner, S. J., Tibolla, O., & Hauser, M. 2011, *A&A*, 534, A130
 Kouch, P. M., Liodakis, I., Middei, R., et al. 2024, *A&A*, 689, A119
 Lefa, E., Rieger, F. M., & Aharonian, F. 2011, *ApJ*, 740, 64
 Lemoine, M., Murase, K., & Rieger, F. 2024, *Phys. Rev. D*, 109, 063006

- Lien, A. Y., Krimm, H. A., Markwardt, C. B., et al. 2025, ApJ, 989, 161
- Liodakis, I., Marscher, A. P., Agudo, I., et al. 2022, Nature, 611, 677
- Mannheim, K. 1993, A&A, 269, 67
- Maraschi, L., Ghisellini, G., & Celotti, A. 1992, ApJ, 397, L5
- Marscher, A. P. 1980, ApJ, 239, 296
- Matsumoto, J., Komissarov, S. S., & Gourgouliatos, K. N. 2021, MNRAS, 503, 4918
- Matsumoto, J. & Masada, Y. 2013, ApJ, 772, L1
- Miller, J. A., Larosa, T. N., & Moore, R. L. 1996, ApJ, 461, 445
- Mizuno, Y., Gómez, J. L., Nishikawa, K.-I., et al. 2015, ApJ, 809, 38
- Mücke, A. & Protheroe, R. J. 2001, Astroparticle Physics, 15, 121
- Oh, K., Koss, M., Markwardt, C. B., et al. 2018, ApJS, 235, 4
- Romero, G. E., Boettcher, M., Markoff, S., & Tavecchio, F. 2017, Space Sci. Rev., 207, 5
- Sbarrato, T., Ajello, M., Buson, S., et al. 2025, Space Sci. Rev., 221, 62
- Sciacaluga, A. & Tavecchio, F. 2022, MNRAS, 517, 2502
- Sciacaluga, A., Tavecchio, F., Landoni, M., & Costa, A. 2024, A&A, 687, A247
- Sikora, M., Begelman, M. C., & Rees, M. J. 1994, ApJ, 421, 153
- Sikora, M., Madejski, G., Moderski, R., & Poutanen, J. 1997, ApJ, 484, 108
- Silva, L., Granato, G. L., Bressan, A., & Danese, L. 1998, ApJ, 509, 103
- Sol, H. & Zech, A. 2022, Galaxies, 10, 105
- Tavecchio, F., Ghisellini, G., Ghirlanda, G., Foschini, L., & Maraschi, L. 2010, MNRAS, 401, 1570
- Tavecchio, F., Maraschi, L., & Ghisellini, G. 1998, ApJ, 509, 608
- Tavecchio, F., Nava, L., Sciacaluga, A., & Coppi, P. 2025, A&A, 694, L3
- Tomsick, J. & COSI Collaboration. 2022, in 37th International Cosmic Ray Conference, 652
- Vanthieghem, A., Lemoine, M., Plotnikov, I., et al. 2020, Galaxies, 8, 33
- Woo, J.-H., Urry, C. M., van der Marel, R. P., Lira, P., & Maza, J. 2005, ApJ, 631, 762
- Zech, A. & Lemoine, M. 2021, A&A, 654, A96
- Zhou, Y. & Matthaeus, W. H. 1990, J. Geophys. Res., 95, 14881

Appendix A: Electron and turbulence spectra

Figures A.1 and A.2 show the time evolution of the electron and turbulence spectra of Case A, respectively. Electrons, injected into the downstream region with Lorentz factors in the range $10^3 < \gamma \lesssim 10^5$, are accelerated by the turbulence up to $\gamma \gtrsim 10^7$, where radiative cooling becomes dominant. During the acceleration, electrons extract energy from the turbulence, leading to strong damping at wavenumbers corresponding to the Lorentz factors where acceleration is most efficient. At lower wavenumbers, where the turbulence cascade dominates over electron damping, turbulence follows the standard Kolmogorov spectrum. The damping has further consequences. Initially, electrons tend to accumulate at high Lorentz factors. However, as the turbulence is progressively damped, the acceleration efficiency decreases. Consequently, at later times, the injected population becomes dominant again, flattening the spectrum at low Lorentz factors.

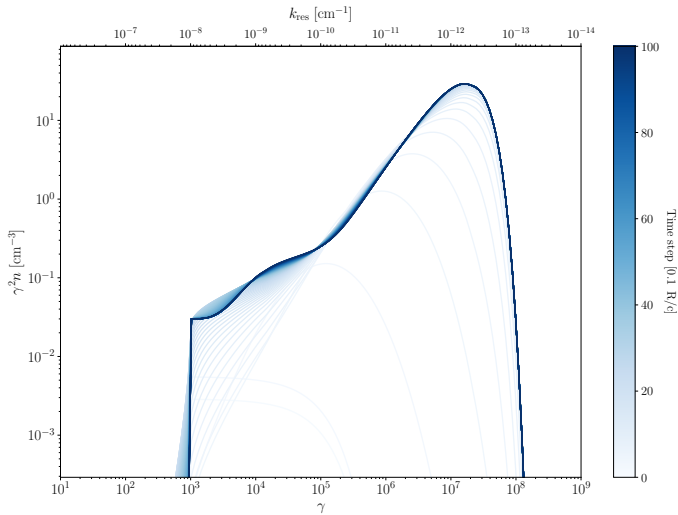


Fig. A.1. Time evolution of the electron number density per unit of Lorentz factor as function of Lorentz factor. The top axis reports the corresponding resonant wavenumber.

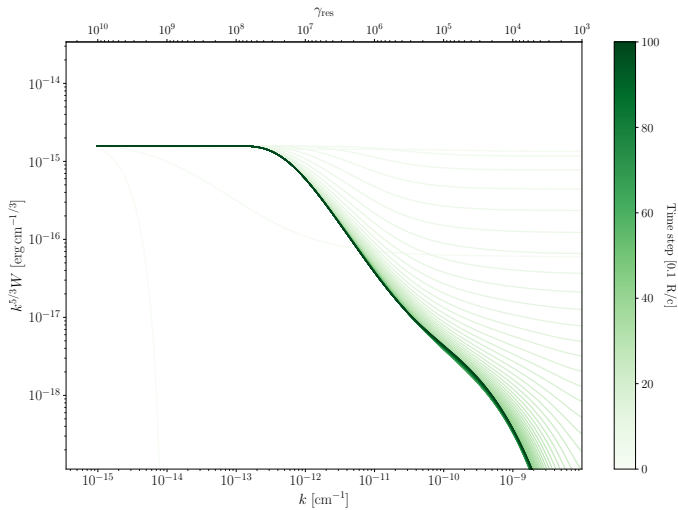


Fig. A.2. Time evolution of the turbulence energy density per unit of wavenumber as function of wavenumber. The top axis reports the corresponding resonant Lorentz factor.

Appendix B: BAT candidates

Table B.1. Candidate BAT sources with their corresponding right ascension (RA), declination (Dec), observed flux, photon index, and catalogs association class.

BAT Name	RA [deg]	Dec [deg]	Flux [10^{-12} erg cm $^{-2}$ s $^{-1}$]	Photon index	Catalogs association class
SWIFT J0007.8-4133*	1.9545	-41.3559	$10.61^{+1.95}_{-1.52}$	$1.41^{+0.50}_{-0.51}$	No archival soft X-ray image
SWIFT J0656.0-6560*	103.989	-65.9981	$10.02^{+1.52}_{-1.16}$	$1.42^{+0.49}_{-0.49}$	No archival soft X-ray image
SWIFT J0722.5+2121	110.668	21.4408	$12.03^{+2.02}_{-1.61}$	$1.21^{+0.61}_{-0.63}$	No soft X-ray detection
SWIFT J1334.1-3842	203.437	-38.4501	$14.17^{+5.57}_{-4.19}$	$1.35^{+0.47}_{-0.48}$	No archival soft X-ray image
SWIFT J0045.9+3931	11.5092	39.531	$11.95^{+3.88}_{-3.58}$	$1.27^{+0.47}_{-0.46}$	No likely soft X-ray counterpart
SWIFT J0106.1+4818	16.5232	48.2949	$11.59^{+3.71}_{-3.42}$	$1.32^{+0.42}_{-0.43}$	Possible Blazar
SWIFT J0243.2-0553*	40.8043	-5.8867	$10.6^{+1.12}_{-0.61}$	$1.48^{+0.53}_{-0.52}$	Unavailable/unchecked soft X-ray image or crowded region
SWIFT J0449.3+6356	72.3282	63.9334	$14.12^{+3.93}_{-3.61}$	$1.38^{+0.39}_{-0.40}$	No likely soft X-ray counterpart
SWIFT J1026.3+4536	156.586	45.5992	$10.75^{+3.53}_{-3.23}$	$1.26^{+0.46}_{-0.47}$	Unavailable/unchecked soft X-ray image or crowded region
SWIFT J1949.7-3636*	297.436	-36.5979	$14.07^{+4.04}_{-3.71}$	$1.49^{+0.41}_{-0.41}$	Unavailable/unchecked soft X-ray image or crowded region

Notes. Further details on the counterpart association procedure followed by the catalogs are available in Section 2.1 of [Oh et al. 2018](#) and Section 2 of [Lien et al. 2025](#). An asterisk (*) marks sources for which a possible soft X-ray counterpart was identified upon the further inspection of archival data described in the text.

We further checked the existence of soft X-ray counterparts for these 10 sources using archival images and catalogs provided by Swift-XRT, Chandra, XMM-Newton, ROSAT, and eROSITA. We confirm the absence of any likely X-ray counterpart for all sources except 4, which show a non-negligible association probability with sources characterized by X-ray fluxes close to the limiting value defined by [Lien et al. \(2025\)](#). Specifically, SWIFT J0007.8-4133 lies 8 arcmin from MCG-07-01-011, a Seyfert 2 galaxy detected by XMM-Newton, Swift-XRT, and eROSITA; SWIFT J0656.0-6560 is 6 arcmin from Fairall 0265, a Seyfert 1 galaxy detected by ROSAT and Swift-XRT; SWIFT J0243.2-0553 is located 2.3 arcmin from the known γ -ray emitting blazar PKS 0240-060; and SWIFT J1949.7-3636 is close to a ROSAT-detected source with no identified optical counterpart.